Supporting Information

A Critical Intermediate Structure that Directs the Crystalline Texture and Surface Morphology of Organo-Lead Trihalide Perovskite

Hao-Chung Chia,[1,#] *Hwo-Shuenn Sheu,*[2,#] *Yu-Yun Hsiao,*[3] *Shao-Sian Li,*[3] *Yi-Kang Lan,*[4] *Chung-Yao Lin,*[1] *Je-Wei Chang,*[1] *Yen-Chien Kuo,*[2] *Chia-Hao Chen,*[2] *Shih-Chang Weng,*[2] *Chun-Jen Su,*[2] *An-Chung Su,*[1] *Chun-Wei Chen*[*3] *& U-Ser Jeng*[1,2,*]

[1] Department of Chemical Engineering, National Tsing Hua University, Hsinchu 30013, Taiwan

[2] National Synchrotron Radiation Research Center, Hsinchu Science Park, Hsinchu 30076, Taiwan

[3]Department of Materials Science and Engineering, National Taiwan University, Taipei 10617, Taiwan.

[4]Materials and Electro-Optic Research Division, National Chung-Shan Institute of Science and Technology, Taoyuan 32546, Taiwan

[#]these two authors contribute equally

Corresponding Authors;

[*]E-mails: chunwei@ntu.edu.tw

[*]E-mail: usjeng@nsrrc.org.tw

- **Grazing-Incidence X-ray Scattering (GIXS).** The as-cast sample thin films were sealed respectively in a vacuum-tight sample chamber with N_2 flow for GIXS conducted at the BL23A SWAXS instrument of Taiwan Light Source (TLS) of the National Synchrotron Radiation Research Center (NSRRC), Hsinchu[s1]. An X-ray beam of 15 keV, with an incident angle of 2.0°, was used in GIXS data collection with 500 ms time-resolution, during in situ annealing at 100, 110, or 120 °C. Data were collected using a CMOS flat panel detector C10158DK-3957, of a pixel size of 50 μm, and a sample-to-detector distance of 192 mm. With the sample surface defined as the *x*-*y* plane and the incident x-rays in the *x*-*z* plane, the scattering vector $\boldsymbol{q}$ = (q_x, q_y, q_z) can expressed as $q_x = 2\pi\lambda^{-1}(\cos\beta\cos\phi - \cos\alpha)$, $q_y = 2\pi\lambda^{-1}(\cos\beta\sin\phi)$, and $q_z = 2\pi\lambda^{-1}(\sin\alpha + \sin\beta)$, with α and β for the incident and exit angles and ϕ for the scattering angle away from the y-z plane (Figure S-1)[s1]. The in-plane and out-of-plane scattering vector are respectively defined by q_r and q_z, with $q_r = (q_x^2 + q_y^2)^{1/2}$. The scattering peak positions were calibrated rigorously with the diffraction peaks from powders of Si, silver-behenate, and LaB_6. The typical data collection time was 500 ms/frame.

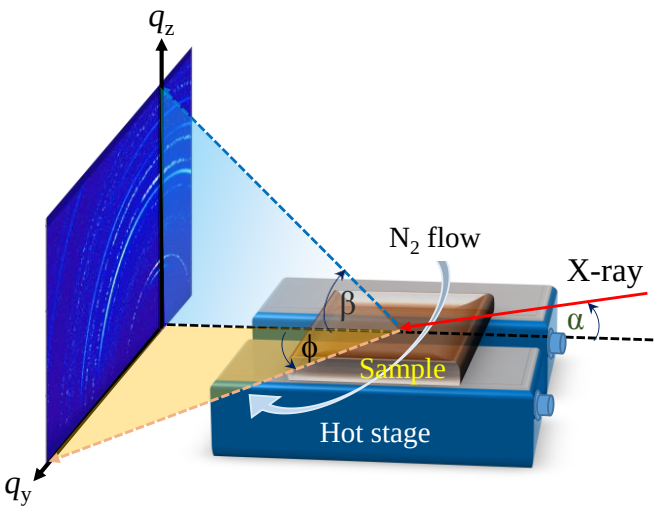

Figure S-1. Schematic view of the GIXS setup. The beam incident and scattering angles are α, β, and ϕ, as indicated.

- **X-ray Photoelectron Spectroscopy (XPS)**

The synchrotron radiation based high-resolution XPS measurements were carried out at the beamline 09A1 of TLS of NSRRC. The experimental station is equipped with an ultra-high sample vacuum system (base pressure better than 5×10^{-10} mbar) and a hemispherical electron energy analyzer (Model 10-360, PHI). All the XPS spectra were taken at a 54° take-off angle with an incident beam of 770 eV. The photon energy was calibrated by Au 4f core level signal emitted from a clean Au thin film that was electrically contacted with the samples. The overall spectra energy resolution is better than 100 meV[s2]. The measurements were carried out at room temperature.

- **X-ray Refinement of the Intermediate Structure**

Simulation of the intermedia phase $\boldsymbol{L}_1$ was based on the single crystal structure of (EDBE)[PbI_4] where EDBE is for 2,2′-(ethylenedioxy)bis(ethylammonium).[s3-s4] The (EDBE)[PbI_4] has a monoclinic structure of a space group $P2_1/c$, with the lattice parameters a = 6.4940(5) Å , b = 29.461(2) Å , c = 9.2666(7) Å , and β = 91.777(2)°. The structure contains (101) inorganic sheets with pronounced distortion from octahedral geometry around the Pb^{II} centers. The organic solvent molecule EDBE was co-crystallized between inorganic sheets. Along the *a*-*c* plane, the $[PbI_6]^{4-}$ octahedra form inorganic polyhedral sheets with shared corners for the 2D perovskite structure. We modified this (EDBE)[PbI_4] structure for the intermediate phase $\boldsymbol{L}_1$ of $MA_2PbI_2Cl_2$·MAI, by replacing the octahedral $[PbI_6]^{-4}$ with $[PbI_4Cl_2]^{4-}$ and EDBE with MAI (methyl ammonium iodide). Moreover, a layer of MAI is introduced in-between the perovskite layers for a centrosymmetric bilayer structure. In the MAI layer, the iodine ions less influenced by the Cl ions of the octahedra were found to deviate slightly from the bilayer center line (cf. Figure S-2d) for best-fit of the X-ray data (Figure S-2a,c). Due to symmetry constraint of Z = 4 in crystallographic general position, the corresponding occupancy of these fluctuated iodine ions is assigned to be 0.25. The hence optimized $\boldsymbol{L}_1$ crystal structure using the DASH program [s5-s6] is of the same space group of $P2_1/c$, with Pawley-method refined unit cell parameters shown in Table S-1. The simulation powder XRD profiles shown in Figure S-2d (marked as modified simulation; same as that in Figure 1b) is obtained by the GSAS program with a preferred orientation along the lattice *b* direction (film normal)[s5-s6] using the proposed crystal structure refined with energy minimization for optimized MA positions (as detailed below). The spherical preferred orientation factor R_o used is 1.25 along the [010] direction of the $\boldsymbol{L}_1$ phase (note that R_o =1 for isotropic orientation). A large Debye Waller factor dominated by the mean square displacement $\langle u^2 \rangle$ ~0.063 $Å^2$ of the heavier atoms of lead and iodine was also included in the crystal structure refinement (cf. Figure S-2e), which accounts for increasingly larger peak intensity damping in higher-*q* region at the 110 °C annealing.

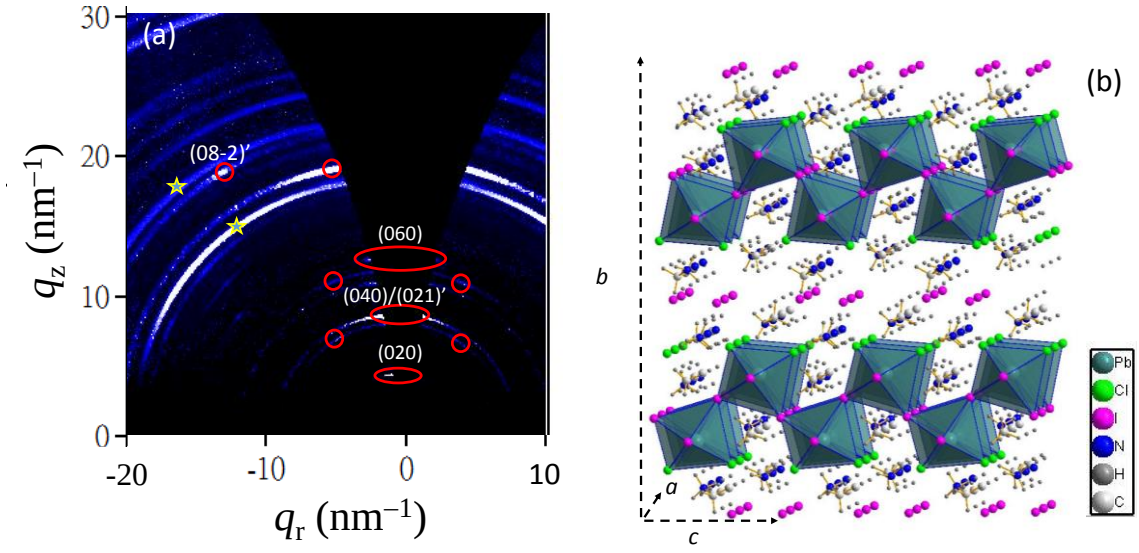

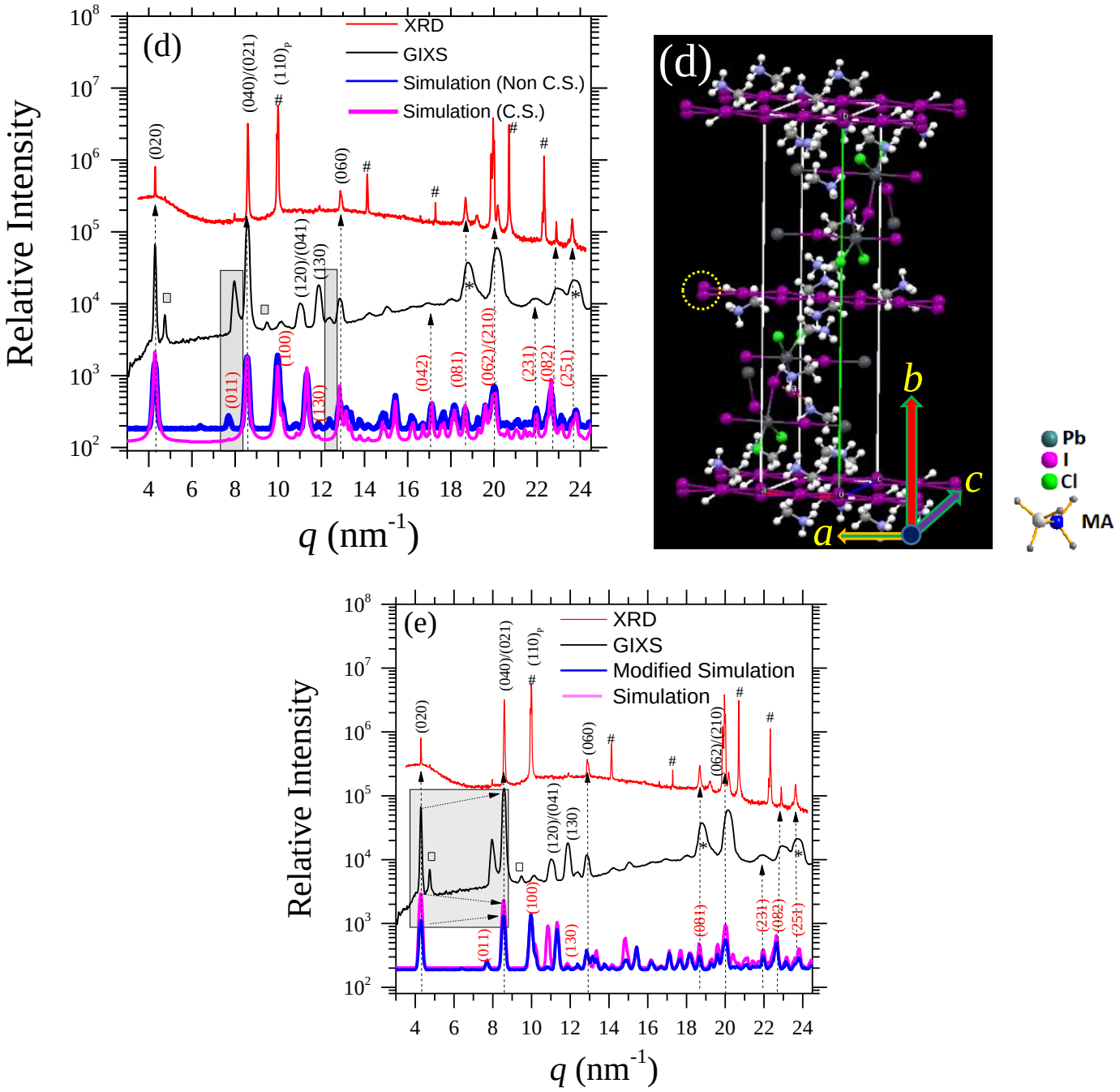

Figure S-2. (a) GIXS pattern corresponding to that shown in Figure 1a, corrected (with a missing wedge along the q_z direction) with the GIXS geometry (with a flat 2D detector) for rigorously defined out-of-plane and in-plane scattering vector q_z and q_r, as detailed in a previous report.[s7] The reflections are indexed according to the proposed $\boldsymbol{L}_1$ crystal structure. The symbol * marks the reflections from FTO. **(b)** Crystal structure for the intermediate phase $\boldsymbol{L}_1$ with the lattice vectors ***a***, ***b***, and ***c***. The octahedra stack along the crystallographic ***a*** vector, with the 2D perovskite layers in the ***a-c*** plane. Filling in-between the perovskite layers are the CH_3NH_3I (MAI) layers. (c) The GIXS profile fitting is improved (as indicated by the shaded squares) with iodine ions of the central MAI layer in the unit cell deviating from the centrosymmetric (C.S.) position of the bilayer structure by ca. 0.3 Å with 50% probability to each side, as representatively indicated by the dotted circle shown in (d). (e) The GIXS profile fitting is further improved for relative intensities of the (020) and (040) peaks (as

indicated by the shaded squares and dotted arrows) by including in preferred orientation and Debye Waller factor (indicated as Modified Simulation), compared to that without (marked as Simulation).

Table S-1. Lattice parameters of $\boldsymbol{L}_1$ phase and perovskite. For the $\boldsymbol{L}_1$ phase, a preferred orientation R_o = 1.25 in [0*l*0] planes and a Debye Waller factor dominated by $\langle u^2 \rangle$ ~0.063 Å^2 of the heavier atoms of Pb and I are used in structural optimization.

Lattice parameter	a (Å)	b (Å)	c (Å)	α (°)	β (°)	γ (°)
$\boldsymbol{L}_1$ (Monoclinic)	6.30	29.35	8.49	90	92.1	90
Perovskite (Cubic)	6.22	6.22	6.22	90	90	90
Perovskite (Tetragonal)	8.914	8.914	12.716	90	90	90

- **Cross-Section TEM Image of the Perovskite $MAPbI_{3-x}Cl_x$ (with $x \approx 0$)**

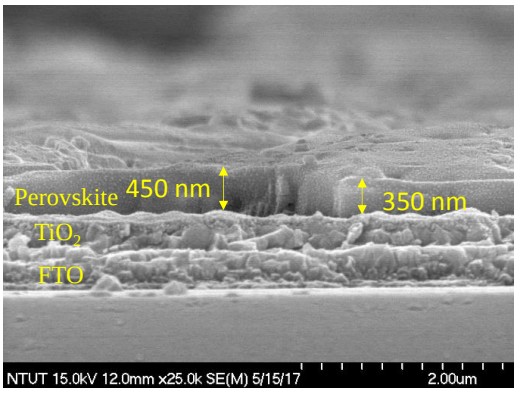

Figure S-3. A cross-section TEM image revealing a similarly processed perovskite layer ($MAPbI_{3-x}Cl_x$) of about 400 ± 50 nm on top of a compact TiO_2 layer ca. 200 nm in thickness, above the FTO glass substrate layer (ca. 200 nm).

- **Energy Minimization for the MA Positions in the $\boldsymbol{L}_1$ Phase**

All the *ab initio* calculations with the X-ray determined crystal structure of $\boldsymbol{L}_1$ were carried out using a projector augmented wave method within the framework of the Perdew-Wang-type [s8] generalized gradient approximation (the GGA-PW91), using the software package CASTEP[s9]; in which, OBS is implemented as the dispersion corrections[s10] of the density functional theory. The presence of tightly bound core electrons is represented by a nonlocal ultrasoft pseudopotential and the tolerance in the self-consistent field (SCF) calculation is 5.0×10^{-7} eV/atom. The BFGS[s11] scheme was used for the system geometry optimization to reach the convergence tolerances of the energy (5.0×10^{-6} eV/atom), maxima force (0.01eV/Å), maxima stress (0.02 GPa) and displacement (5.0×10^{-4} Å). The geometry optimization was performed based on the lattice parameters and atomic sites of the crystal structure obtained from the X-ray data. The hence optimized MA positions are mostly in hydrogen bonding range with the inorganic octahedra (Figure S-4).

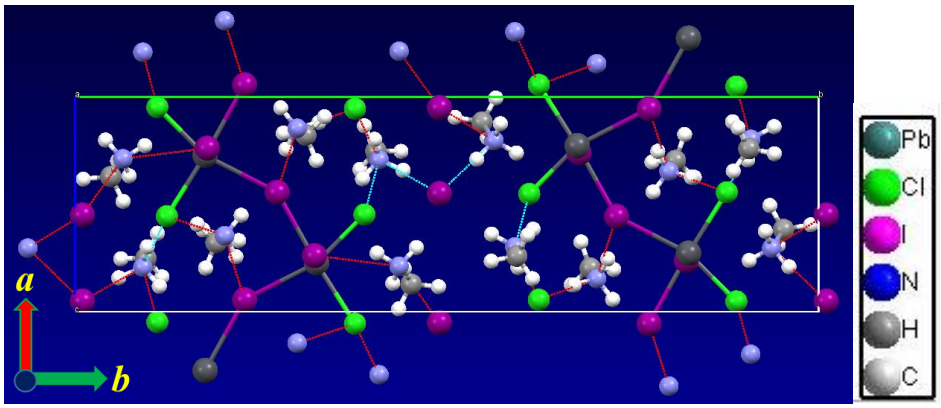

Figure S-4. The $\boldsymbol{L}_1$ structure with the MA positions optimized with energy minimization. The thin dotted (red) lines illustrate hydrogen bonding range between MA and the halides of the octahedra.

- **More About the $\boldsymbol{L}_1$ phase.**

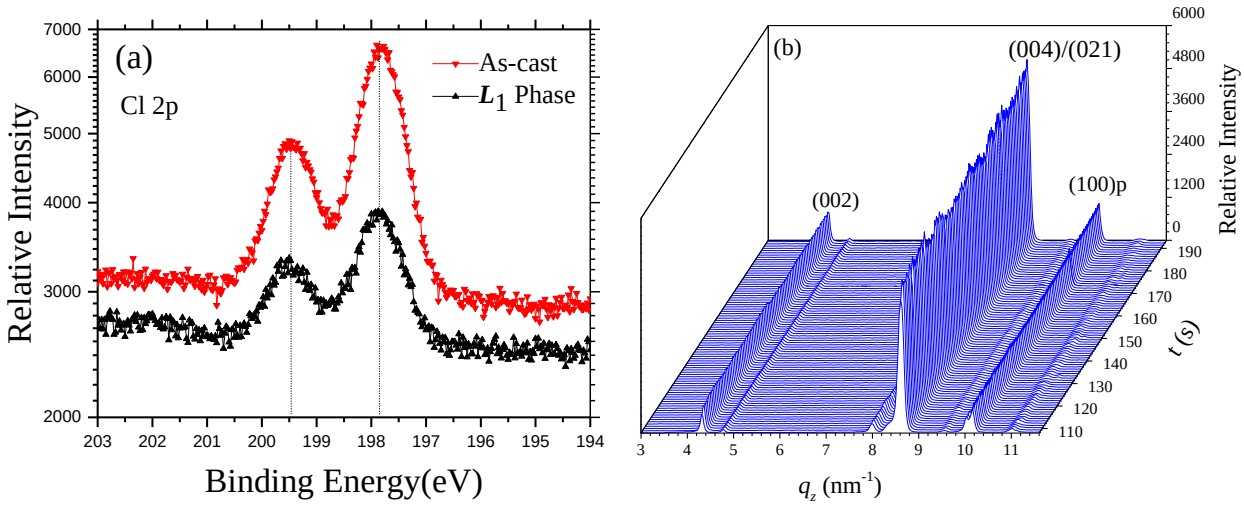

Figure S-5. (a) Similar XPS core level spectra of Cl 2p for the as-cast film and that annealed for pure $\boldsymbol{L}_1$ phase, after spin-cast from a DMF solution of MAI and $PbCl_2$ (3:1 molar ratio). The result suggests that similar Cl-incorporated lead-halide octahedra of $[PbI_4Cl_2]^{-4}$ were already formed in the as-cast film. (b) Largely saturated intensities of the (002) and (004)/(021) reflections of the $\boldsymbol{L}_1$ phase during t = 100 to 200 s of the 110 °C annealing, supplemental to that shown in Figure 3a,b.

- **Intensity and Size Evolutions of the L_1 Phase.**

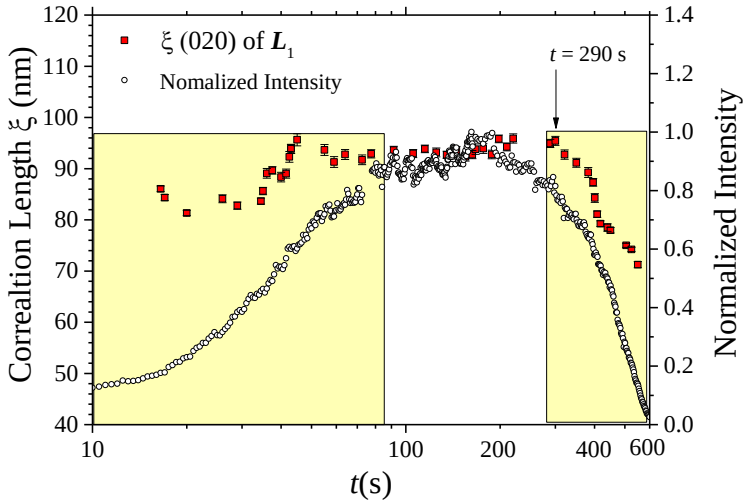

Figure S-6. The intensity and size evolutions of the $\boldsymbol{L}_1$ phase at 110 °C annealing, extracted from the $\boldsymbol{L}_1$ (020) reflection in Figure 3a,b. The arrow at t = 290 s indicates initiation of the decays of the intensity and size, coinciding with the beginning of the intensity growth of perovskite with the Avrami exponent n = 2.55 shown in Figure 4c. The matured size of ξ (~100 nm) measured at high temperature 110 °C annealing with GIXS is significantly smaller than the 250 nm measured with high-resolution XRD (cf. Figure 1b), after the sample ($\boldsymbol{L}_1$ phase) cooled down to ambient temperature.

- **Cubic-to Tetragonal Phase Transition**

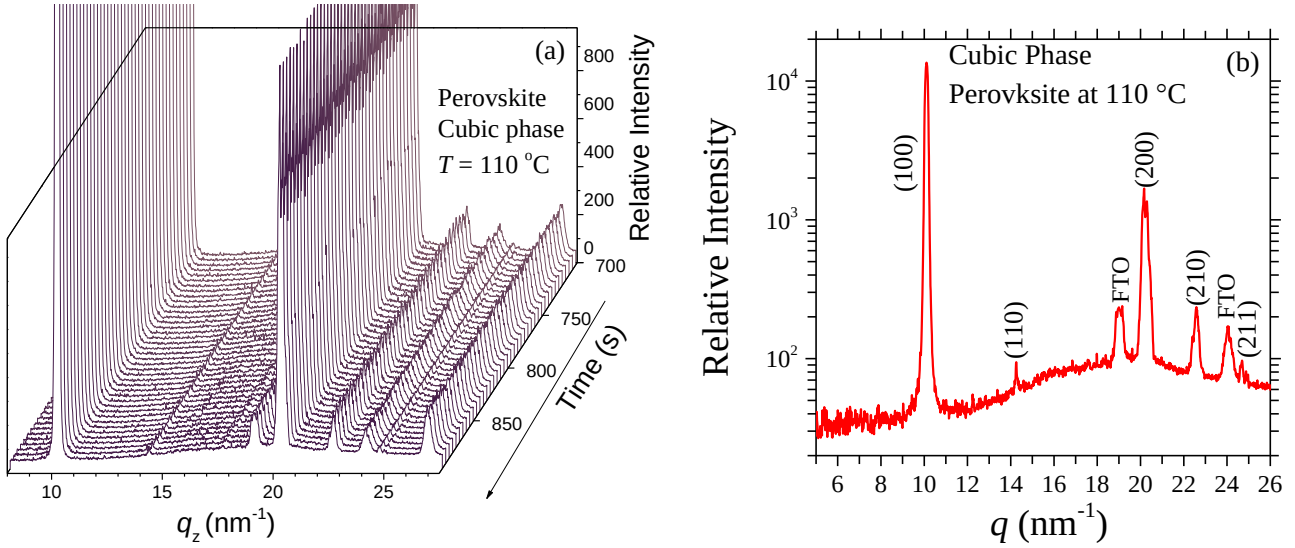

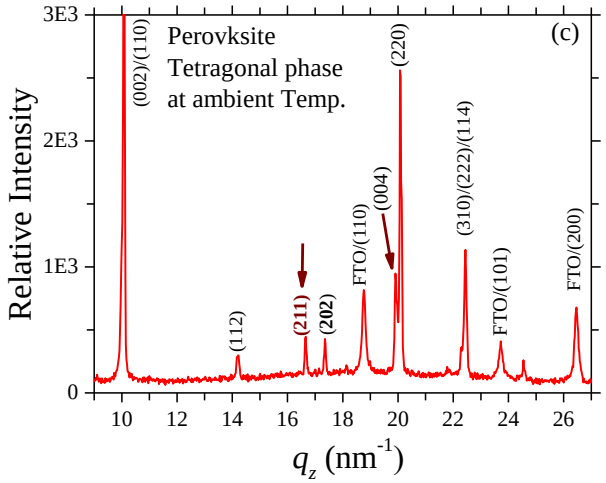

Figure S-7. (a) Time-resolved GIXS profiles taken along the vertical direction of the corresponding 2D patterns measured after the $\boldsymbol{L}_1$-to-perovskite conversion at 110 °C for $MAPbI_{3-x}Cl_x$ (with x~0). (b) A typical spectrum from (a) with the reflection peaks assigned using an oriented cubic (100) crystal structure of perovskite, with a refined lattice constant 6.220 Å (Table S-1). (c) A corresponding XRD profile after the sample cooled down to ambient temperature for the cubic-to-tetragonal phase transition. The reflections are indexed according to a tetragonal phase, with lattice constants shown in Table S-1. The thick arrows mark out the appearance of the characteristic reflections after the cubic-to-tetragonal phase transition [s12-s13].

- **Crystal Orientation of Perovskite Formed in an As-Spun Film from MAI and PbI_2.**

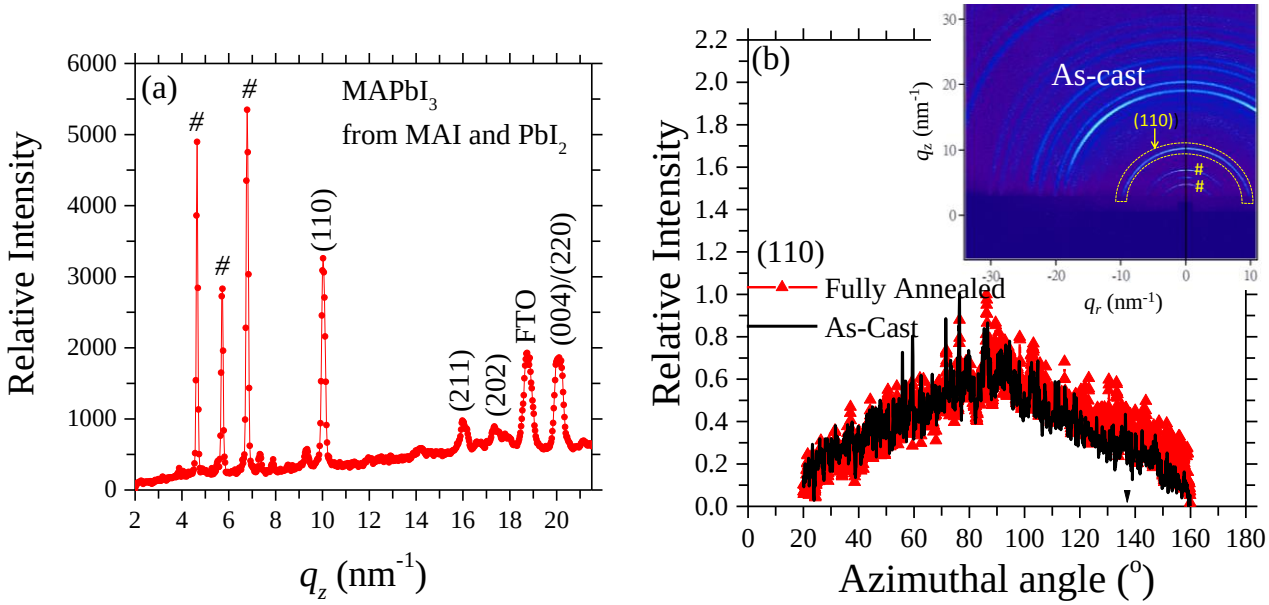

Figure S-8. (a) GIXS profile for the as-cast film processed from a DMF solution containing all iodine ingredients of MAI and PbI_2 (molar ratio 3:1). The peaks are indexed using a tetragonal lattice for perovskite; symbol # marks the reflections from an intermediate phase, differing from the $\boldsymbol{L}_1$ phase of Cl ions incorporated. (b) The corresponding 2D pattern (inset) for the as-cast film. The representative powder ring of perovskite (110) reflection indicates largely randomly oriented perovskite crystals, coexisting with the

oriented intermediate structure (reflections marked with #) in the as-cast film. Also shown are the wide-spread intensity distribution profiles of the (110) reflection as a function of the azimuthal angle (90 ° for the film normal) for the as-cast and fully annealed films, with a generally preferred orientation in the film normal.

References:

(S1) Wu, W.-R.; Su, C.-J.; Chuang, W.-T.; Huang, Y.-C.; Yang, P.-W.; Lin, P.-C.; Chen, C.-Y.; Yang, T.-Y.; Su, A.-C.; Wei, K.-H. Surface Layering and Supersaturation for Top-Down Nanostructural Development during Spin Coating of Polymer/Fullerene Thin Films, *Adv. Energy Mater.* **2017**, 7, 1601842–1601853.

(S2) Lou, J. L.; Shiu, H. W.; Chang, L. Y.; Wu, C. P.; Soo, Y.-L.; Chen, C.-H. Preparation and Characterization of an Ordered 1-Dodecanethiol Monolayer on Bare Si(111) Surface, *Langmuir* **2011**, 27, 3436–3441.

(S3) Dohner, E. R.; Jaffe, A.; Bradshaw, L. R.; Karunadasa, H. I. Intrinsic White-Light Emission from Layered Hybrid Perovskites. *J. Am. Chem. Soc.* **2014**, 136, 13154–13157.

(S4) Dohner, E. R.; Hoke, E. T.; Karunadasa, H. I. Self-Assembly of Broadband White-Light Emitters. *J. Am. Chem. Soc.* ***2014***, 136, 1718−1721.

(S5) David, W. I.; Shankland, K.; van de Streek, J.; Pidcock, E.; Motherwell, W. S.; Cole, J. C. DASH: A Program for Crystal Structure Determination from Powder Diffraction Data, *J. Appl. Crystallogr.* **2006**, 39, 910-915.

(S6) Larson, A. C.; Von Dreele, R. B. Gsas. General Structure Analysis System. *LANSCE, MS-H805, Los Alamos, New Mexico* **1994**.

(S7) Baker, J. L.; Jimison, L. H.; Mannsfeld, S.; Volkman, S.; Yin, S.; Subramanian, V.; Salleo, A.; Alivisatos, A. P.; Toney, M. F. Quantification of Thin Film Crystallographic Orientation Using X-Ray Diffraction With an Area Detector. *Langmuir* **2010,** *26*, 9146-9151.

(S8) Perdew, J. P.; Chevary, J. A.; Vosko, S. H.; Jackson, K. A.; Pederson, M. R.; Singh, D. J.; Fiolhais, C. Atoms, molecules, solids, and surfaces: Applications of the Generalized Gradient Approximation for Exchange and Correlation, *Phys. Rev. B*, **1992**, 46, 6671–6687.

(S9) Ortmann, F.; Bechstedt, F.; Schmidt, W. Semiempirical van der Waals Correction to the Density Functional Description of Solids and Molecular Structures, *Phys. Rev. B* **2006**, 73, 205101.

(S10) Clark, S. J.; Segall, M. D.; Pickard, C. J.; Hasnip, P. J.; Probert, M. I.; Refson, K.; Payne, M. C. First Principles Methods using CASTEP, *Zeitschrift fuer Kristallographie* **2005**, 220, 567-570.

(S11) Pfrommer, B. G.; Côté, M.; Louie, S. G.; Cohen, M. L. Relaxation of Crystals with the Quasi-Newton Method, *J. Comput. Phys.* **1997**, 131, 133-140.

(S12) Li, S.-S.; Chang, C.-H.; Wang, Y.-C.; Lin, C.-W.; Wang, D.-Y.; Lin, J.-C.; Chen, C.-C.; Sheu, H.-S.; Chia, H.-C.; Wu, W.-R. Intermixing-Seeded Growth for High-Performance Planar Heterojunction Perovskite Solar Cells Assisted by Precursor-Capped Nanoparticles. *Energy Environ. Sci.*, **2016**, 9, 1282-1289.

(S13) Luo, S.; Daoud, W. A. Crystal Structure Formation of $CH_3NH_3PbI_{3-x}Cl_x$ Perovskite, *Materials* **2016**, 9, 123–135.